Terr. Atmos. Ocean. Sci., Vol. 30, No. 3, 377-387, June 2019 doi: 10.3319/TAO.2018.11.15.03

The kinematic source analysis for 2018 M_w 6.4 Hualien, Taiwan earthquake

Yi-Ying Wen[1, *], Strong Wen[1], Yuan-Hsi Lee[1], and Kuo-En Ching[2]

[1] *Department of Earth and Environmental Sciences, National Chung Cheng University, Chia-yi County, Taiwan*
[2] *Department of Geomatics, National Cheng Kung University, Tainan City, Taiwan*

Article history:
Received 19 July 2018
Revised 12 November 2018
Accepted 15 November 2018

Keywords:
2018 Hualien earthquake, Kinematic source analysis, Rupture velocity variation

Citation:
Wen, Y.-Y., S. Wen, Y.-H. Lee, and K.-E. Ching, 2019: The kinematic source analysis for 2018 M_w 6.4 Hualien, Taiwan earthquake. Terr. Atmos. Ocean. Sci., 30, 377-387, doi: 10.3319/TAO.2018.11.15.03

ABSTRACT

The 2018 M_w 6.4 Hualien earthquake struck the eastern Taiwan and caused serious damage. We investigate the rupture properties of the 2018 Hualien earthquake by inverting teleseismic body wave and forward modeling GPS coseismic deformation. The rupture process and slip pattern of preferred model explain both the far-field (teleseismic data) and near-field (GPS) observations. The results show that the 2018 Hualien mainshock ruptured southward on two fault segments, with a weak but fast initiation (3.0 km s^{-1}) in the main west-dipping segment F1 and slow (2.0 km s^{-1}) yet significant slip on shallow east-dipping segment F2. In the past few years, several moderate-sized events, which struck eastern Taiwan and caused strong ground shaking and some seismic damage, are considered occurring on the west-dipping fault. Additional investigations are required to building up the knowledge of this not well-known region.

1. INTRODUCTION

On 4 February 2018, one M_w 6.1 event occurred in the offshore area of Hualien City, which is the largest city in the eastern Taiwan. Two days later, the 6 February 2018 M_w 6.4 Hualien earthquake struck the eastern Taiwan and triggered several large aftershocks ($M_w \geq 5.0$) within 24 hr, as shown in Fig. 1. The M_w 6.4 mainshock is also located in the northern offshore area of Hualien City, and the aftershock sequence and strong ground shaking extended toward the northern part of Longitudinal Valley (LV) with the maximum intensity of 7 (> 250 gals) and caused serious damage, including 17 fatalities, 285 injuries, and 4 collapsed buildings. Most damage coincided with the surface rupture zones along the Milun fault (MLNF) and Linding fault (LDNF). The latest severe seismic disaster around Hualien City area was caused by the 1951 Longitudinal Valley earthquake sequence, and the surface ruptures along MLNF were also observed (Hsu 1962; Chen et al. 2008).

According to the Global Centroid Moment Tensor (CMT), Central Weather Bureau (CWB) CMT and the Real-time Moment Tensor monitoring system (RMT, Lee et al. 2013) solutions, the 2018 Hualien earthquake shows the focal mechanism with a west-dipping fault plane (Fig. 1). However, the MLNF and LDNF, which are observed surface ruptures for the 2018 Hualien event, are considered as the east-dipping faults with high angles (Shyu et al. 2016). In addition, the Global CMT solution suggests an oblique thrust faulting mechanism with a significant non-double-couple component of 61% from the W-phase solution, indicating that the 2018 Hualien event cannot be well represented by a single point source and may involve slip vector variations or multiple rupture planes during the faulting. In this study, we carried out teleseismic waveform inversion and near-field GPS (Global Positioning System) forward modeling to investigate the rupture properties of the 2018 Hualien earthquake.

2. TELESEISMIC WAVEFORM INVERSION

Here, we set up a simplified finite-fault geometry based on the focal mechanism, the field observations and aftershock distribution. As shown in Fig. 1, focal mechanism

* *Corresponding author*
E-mail: yiyingwen@ccu.edu.tw

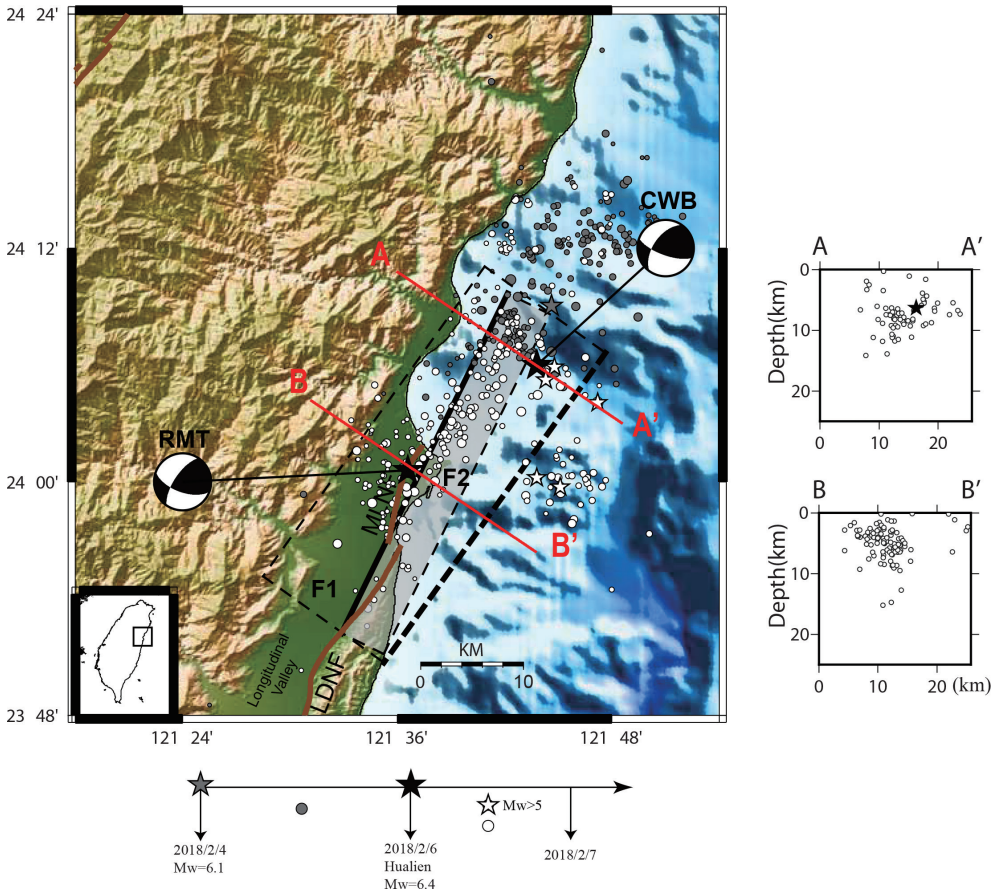

Fig. 1. Locations and focal mechanisms for the 2018 Hualien earthquake and the seismicity from 2018/2/4 to 2018/2/7 recorded by CWB. The stars indicate locations of the 2018/2/4 M_w 6.1 event (gray), the 2018 M_w 6.4 Hualien earthquake (black), and its large aftershocks with $M_w \geq 5$ (white). The seismicities at the different time periods are marked with different color dots. The dashed rectangles show the locations of two fault segments.

and aftershock distribution (AA' profile) both suggested a west-dipping fault plane. However, based on the geological investigation (Chen 2018), the surface ruptures were observed along the east-dipping Milun fault trace and the aftershocks occurred on the southern part (BB' profile) also indicated an east-dipping segment. Therefore, two possible fault segments are considered: (1) F1: a 36-km west-dipping segment oriented N215°E with a 24-km width (i.e., down-dip extent) dipping 55°, and (2) F2: a 36-km east-dipping segment oriented N26°E with a 9-km width dipping 60°. The fault plane is then divided into finite subfaults, each with a dimension of 3 km × 3 km along the strike and dip directions, respectively. The teleseismic broadband waveforms typically have good data quality and widespread azimuthal coverage, thus providing a good opportunity to investigate the primary characteristics of fault rupture behavior and slip pattern. There are 16 *P*-waves and 8 *SH*-waves from the Data Management Center of the Incorporated Research Institutions for Seismology (IRIS-DMC) stations with epicentral distances between 30 and 90° which are selected for the finite-fault modeling, as shown in Fig. 2. The records from 5 s before to 35 s after the *P*- and *S*-wave arrivals with a sampling rate of 0.1 s were used and integrated to displacement after removing the instrument response from the original velocity seismograms and bandpass filtering the data between 0.01 and 0.5 Hz. We applied the generalized ray theory method (Langston and Helmberger 1975), with the 1-D crustal velocity structure of CRUST2.0 (Bassin et al. 2000), to generate teleseismic Green's functions.

For a given station, the seismic record can be represented as the linear sum of response contributed from each ruptured subfault during the faulting. Applying a non-negative least square inversion (Lawson and Hanson 1974), the observed and synthetic waveforms are represented as a system of linear equations:

$$\begin{pmatrix} A \\ \lambda H \end{pmatrix} x = \begin{pmatrix} b \\ 0 \end{pmatrix} \quad (1)$$

where A is the matrix of teleseismic Green's functions, b is the vector of observed data and x represents the solution matrix of the subfault dislocations. In addition, we also considered the stability constraint matrix, H, e.g., the smoothing

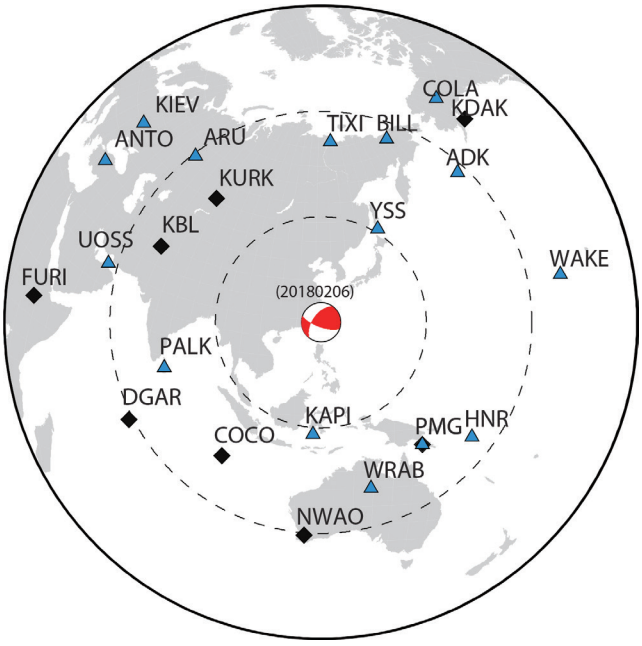

Fig. 2. Teleseismic station distribution. The beach ball indicates the location of the 2018 Hualien earthquake. Triangles and diamonds represent the stations which recorded *P*-wave and *SH*-wave waveforms, respectively, used in this study. The dashed circles represent epicenter distance at a 30-degree interval.

on the slip between adjacent subfaults, with damping ratio, λ. Then, the error is calculated as:

$$\varepsilon = (Ax - b)^2 / b^2 \quad (2)$$

For each subfault, we allow the change in rake direction and use a triangular source-time function with a width of 3 s.

Since the 2018 Hualien earthquake is a moderate-size event, first we carried out the waveform inversion with single fault plane, e.g., a model with segment F1 alone. The optimal model with misfit of ε = 0.331 indicates the 2018 Hualien earthquake ruptured with a slow velocity of 1.6 km s^{-1}. The slip model and comparison of synthetic and observed waveforms are shown in Fig. 3. The total seismic moment is 5.62 × 10^{18} Nm (M_w = 6.44), with the maximum slip of 75.7 cm. This model exhibits a main asperity between the epicenter to the centroid location determined by RMT solution, where is close to the seriously damaged area.

For model with the two fault segments, F1 and F2, we allow the various rupture velocity between 1.0 and 3.2 km s^{-1} on each segment, with an increment interval of 0.2 km s^{-1}. In total, this leads to 144 inverted slip models with various rupture velocities. The asterisk in Fig. 4 represents the optimal model with misfit of ε = 0.325, and it suggests that the 2018 Hualien earthquake initially ruptured with a slow velocity of 1.4 km s^{-1} in segment F1 and propagated to segment F2 with a higher speed of 2.0 km s^{-1}. The total seismic moment is 5.73 × 10^{18} Nm (M_w = 6.44), with the maximum slip of 77.6 cm. The optimal two-faults model (Fig. 5) shows that the main asperity is similar with that of F1-alone model (Fig. 3), but some energy was released on the shallow segment F2 and the location is consistent with surface deformation observed on MLNF and LDNF.

3. GPS FORWARD MODELING

Teleseismic data are frequently used to investigate the primary characteristics of fault rupture behavior and faulting history. However, the long-period nature limits their sensitivity to the detailed complexities of the rupture process. Conversely, the near-field GPS data provides good constraints on the shallow faulting pattern as well as the total rupture area. Since some continuous and campaign GPS stations recorded coseismic offsets of the 2018 Hualien earthquake, we then simulate the static ground displacements using the finite-fault approach of Ji et al. (2002), with a regional 1D velocity structure modified from Kuo-Chen et al. (2012), as listed in Table 1. Coseismic displacements were derived from 24 continuous GPS stations and 16 campaign-mode GPS stations which were announced by the Central Geological Survey, as listed in Tables 2 and 3. Coseismic displacements from continuous GPS stations were estimated by the coordinate difference between three-day average before the event and one-and-half-day average after the earthquake. Because the observations from campaign-mode GPS stations before the earthquake were collected approximately one year ago, the coseismic displacements

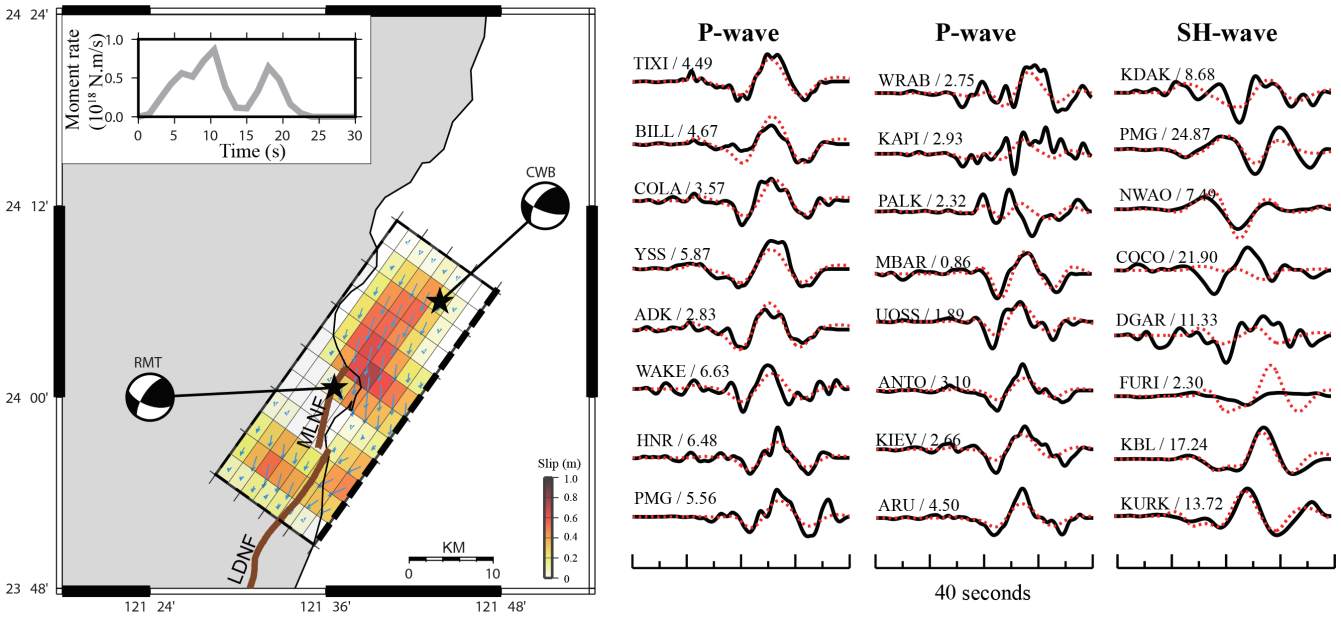

Fig. 3. Slip distribution of the optimal one-fault model (F1) and comparison of the observed (solid line) and synthetic (dashed line) waveforms. The station name and peak value of the record in micrometers are shown above the waveforms.

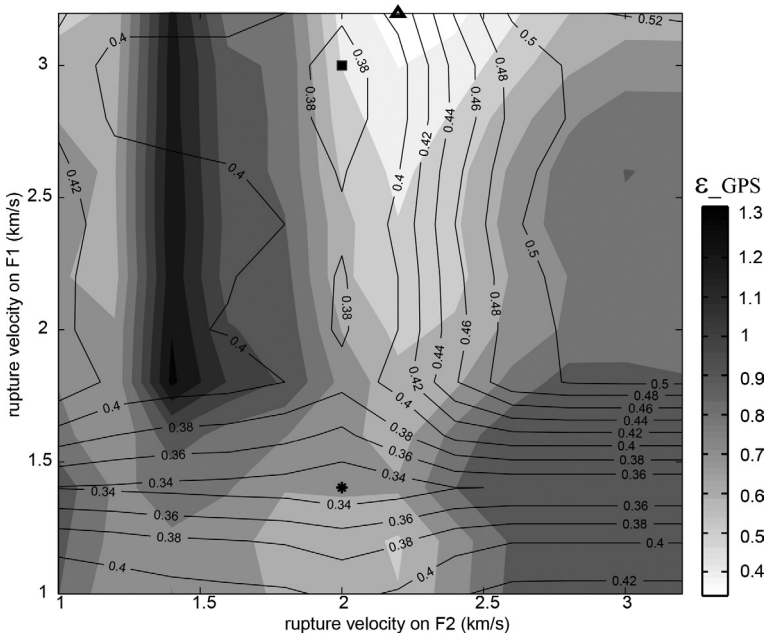

Fig. 4. Misfit of teleseismic waveform inversion (contour) and GPS forward modeling (grayscale) for 144 two-faults model. The asterisk and triangle represent the minimum misfit of teleseismic waveform inversion and GPS modeling, respectively. The square shows a trade-off between waveform inversion and GPS simulation.

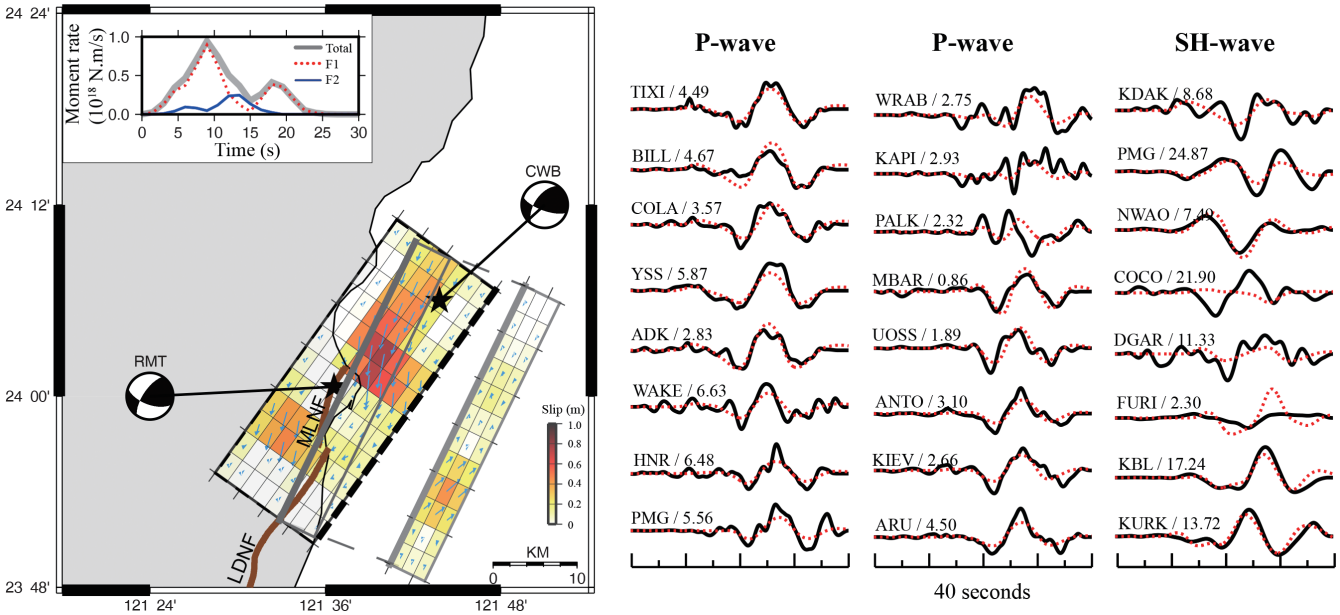

Fig. 5. Slip distribution of the optimal two-faults model and comparison of the observed (solid line) and the synthetic (dashed line) waveforms. The station name and peak value of the record in micrometers are shown above the waveforms.

Table 1. One-Dimensional Velocity Model for GPS Modeling.

Vp (km s^{-1})	Vs (km s^{-1})	Density (g cm^{-3})	Thickness (km)
5.138	2.996	2.391	3
5.648	3.375	2.575	3
5.744	3.446	2.609	3
5.836	3.530	2.643	6
5.886	3.661	2.661	9
6.541	3.899	2.897	12
7.695	4.382	3.312	33

Table 2. Coseismic offsets used in this study recorded at continuous GPS stations.

Station	lon. (deg)	lat. (deg)	E (mm)	N (mm)	U (mm)	stE (mm)	stN (mm)	stU (mm)
CHUN	121.3863	23.4542	-5.3	3.8	6.0	3.5	3.3	4.5
DNFU	121.4755	23.6864	-1.1	14.2	9.0	3.9	3.5	5.0
DSIN	121.3912	23.6325	-5.9	-14.0	99.9	4.9	3.7	5.5
FENP	121.5126	23.5998	29.6	-12.1	69.1	4.5	4.2	6.7
FLNM	121.4466	23.7476	-6.9	-1.5	-2.4	3.0	1.8	2.5
FONB	121.5141	23.5995	-6.0	5.9	8.7	3.5	3.3	4.6
HNSN	121.3013	24.3390	0.6	-8.6	13.7	3.5	3.5	4.8
HUAL	121.6067	23.9767	149.1	434.9	70.4	3.3	3.3	4.6
HUAN	121.2658	24.1448	-4.2	0.7	4.9	4.2	4.1	5.7
HUAP	121.7427	24.3103	-11.6	-4.8	29.7	3.9	3.5	5.3
JSUI	121.4171	23.4933	-4.2	3.9	3.5	3.5	3.3	4.8
JYAN	121.2195	24.2438	-6.9	-2.2	-0.1	3.5	3.3	4.7
KNKO	121.4989	23.4735	-8.8	6.7	10.9	3.5	3.2	4.4
NAAO	121.8034	24.4506	-3.2	1.9	16.9	3.5	3.1	4.4
NDHU	121.5440	23.8985	-91.9	-49.6	36.4	3.5	3.2	4.5
NSAN	121.3760	24.4295	-2.6	-10.7	2.7	3.8	3.8	5.6
PEPU	121.6035	24.0192	-54.0	-261.2	98.1	4.3	3.6	5.3
SCHN	121.6448	24.1291	2.9	-97.4	-7.4	3.5	3.2	4.4
SHUL	121.5559	23.7889	-6.4	24.4	10.2	4.7	4.3	6.2
SICH	121.6476	24.1270	1.0	-97.3	-7.6	3.3	3.1	4.4
SLIN	121.4346	23.8132	-21.1	-2.2	5.6	4.7	4.6	7.0
SOFN	121.5914	23.8716	-19.7	92.7	14.4	3.5	3.3	4.7
WULI	121.3017	24.3536	-3.1	-2.5	18.4	3.9	3.8	5.6
YENL	121.5950	23.9048	-17.4	195.0	-34.4	4.6	4.3	6.0

Table 3. Coseismic offsets used in this study recorded at campaign-mode GPS stations.

Station	lon. (deg)	lat. (deg)	E (mm)	N (mm)	U (mm)	stE (mm)	stN (mm)	stU (mm)
E415	121.5662	24.0058	-124.2	-150.4	50.9	4.3	2.9	4.7
G970	121.5972	23.9267	-7.2	337.2	-52.0	4.5	3.0	4.5
G972	121.5887	23.9265	-315.8	-232.3	163.6	4.5	3.0	4.4
G979	121.5285	23.9463	-115.8	-76.4	7.4	5.1	3.2	4.7
GA37	121.6013	23.9849	-18.4	-285.0	-77.6	4.5	3.0	4.4
GA40	121.5749	24.0049	-108.6	-188.6	40.8	4.3	2.9	4.3
GE46	121.5964	23.9880	77.5	-398.1	-73.9	4.5	2.9	4.4
GE63	121.6120	24.0082	265.3	447.1	120.9	4.3	2.9	4.2
GE64	121.6021	24.0157	-70.3	-288.1	40.5	4.3	2.9	4.2
GA41	121.5853	23.8455	-30.1	70.6	-40.6	4.8	3.3	4.9
E549	121.5338	23.8880	-183.0	-49.5	162.2	5.8	3.9	6.8
GA43	121.5129	23.8856	-69.5	-45.3	-11.4	5.0	3.3	4.6
GE56	121.4916	23.7280	6.4	-5.6	-41.6	5.0	3.4	4.7
GE57	121.4608	23.7557	-8.7	-1.9	-27.0	5.0	3.4	4.7
GE08	121.4380	23.7313	-7.1	-9.3	-37.5	5.0	3.3	4.8
GE55	121.4042	23.7170	4.3	-5.0	-6.1	5.0	3.3	4.8

were derived from the coordinate difference before and after the event and the effect from interseismic velocities were removed in this calculation. Based on the uncertainties of coseismic displacements and first-order pattern of coseismic deformation from continuous and campaign-mode GPS stations, horizontal displacements are reliable but the vertical displacements from campaign-mode GPS stations are relatively suspected. The misfits of synthetic to the observed GPS displacements, denoted as $\varepsilon_{\_GPS}$, is also calculated using the same definition as used for teleseismic data. Figures 6a and b show the synthetic GPS displacements derived from the optimal F1-alone model (Fig. 3) and optimal two-faults model (Fig. 5), respectively. Although the orientations of synthetic displacement are roughly consistent with the GPS observations, the synthetic displacement underestimates the measured displacement. As mentioned in previous section, the optimal two-faults model reveals a minor asperity on the shallow segment F2, which might be related to the better fitting around the northern end of LDNF, .e.g., stations G970, YENL, and SOFN. This indicates that two-faults model can better explain the surface deformation caused by the 2018 Hualien earthquake.

For further validation, we calculated the misfit of GPS modeling for all 144 inverted slip results of two-faults model.

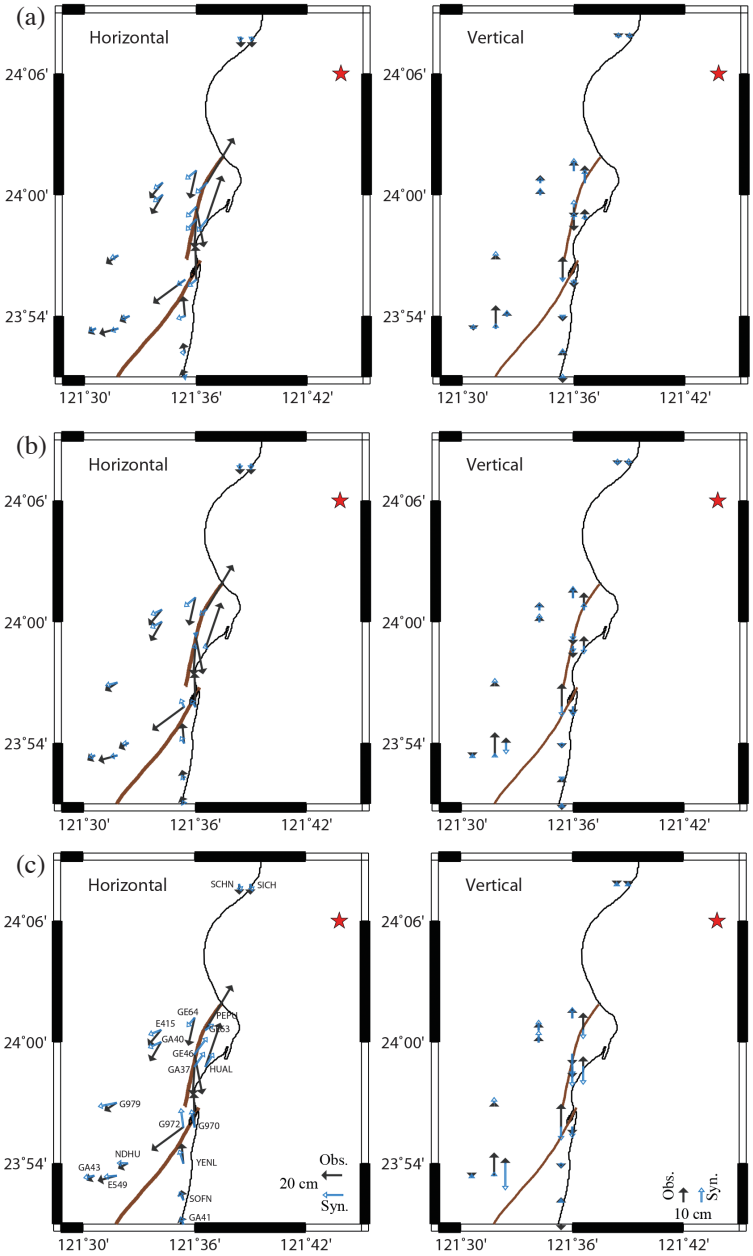

Fig. 6. Modeled horizontal and vertical displacements from (a) optimal F1-alone model, (b) optimal two-faults model, and (c) preferred model, respectively. Solid and open arrows show the observed and synthetic displacements at GPS stations. The asterisk shows the epicenter location.

The open triangle in Fig. 4, which represents the minimum misfit of GPS modeling, indicates a model with fast rupture velocity of 3.2 km s^{-1} in segment F1 and slower speed of 2.2 km s^{-1} in segment F2. Since we adopted a simplified fault geometry, it is not easy to well explain the surface deformation, especially for the near-fault region. Therefore, a trade-off between waveform inversion and GPS simulation is considered, as the square shown in Fig. 4. The synthetic waveforms of the preferred model (Fig. 7) explain the observations well; nevertheless, the slip pattern is significantly different with the other two models. This preferred model of the 2018 Hualien earthquake exhibits a weak initiation with a rupture velocity of 3.0 km s^{-1} in segment F1 and then propagated across F2 at 2.0 km s^{-1}. The total seismic moment is 5.79×10^{18} Nm ($M_w = 6.45$), with the maximum slip of 89.9 cm. In addition, the main asperity was located on segment F2, and the minor asperity ruptured the deeper part of segment F1. The locations of both asperities are concentrated on the seriously damaged area and close to the RMT centroid location. Figure 6c shows the synthetic GPS displacements derived from the preferred model (Fig. 7). With the exception of some very near-fault stations, the synthetic coseismic displacements best explained the amplitudes and orientations of observed GPS cosesmic data.

4. DISCUSSION AND CONCLUSIONS

With the advantages of nice azimuthal coverage and easy accessibility, teleseismic records are popularly used to investigate the earthquake properties. However, due to the limitation of data resolution as well as the simplification of fault geometries, models derived from teleseismic data alone can provide the primary faulting process and slip pattern, especially at greater depths. It means that teleseismic waveform inversion is relatively insensitive to reveal slip patterns at shallow depths. On the other hand, the near-field GPS coseismic deformation data can give better constraints on the shallow rupture pattern. Without any constraint, the optimal results of the one-fault model (F1, Fig. 3) and two-faults model (Fig. 5) both exhibit large amounts of slip at deeper depths, but the synthetic surface displacements do not well fit GPS observations, as shown in Figs. 6a and b, respectively. With the indirect constraint by forward GPS simulation, the preferred model (Fig. 7) shows good fits to both teleseismic and GPS data. For the 2018 Hualien event, there are some continuous GPS stations recorded the coseismic information. Figure 7 also shows the time series records of two near-fault stations, PEPU and HUAL. It is noticed that a significant energy release between 12 - 16 s after the initiation was revealed by station HUAL, and this feature coincides with the main moment-rate burst released on segment F2. It suggests the reliability of the preferred model and also explains the faulting mechanism with a significant non-double-couple component.

In our model, fault segment F2 could represent the MLNF and LDNF, however, the west-dipping fault segment F1 is not identified by Central Geological Survey yet. Chuang et al. (2014) suggested that the 2000 M_L 6.2 Hualien event occurred on the west-dipping Central Range fault,

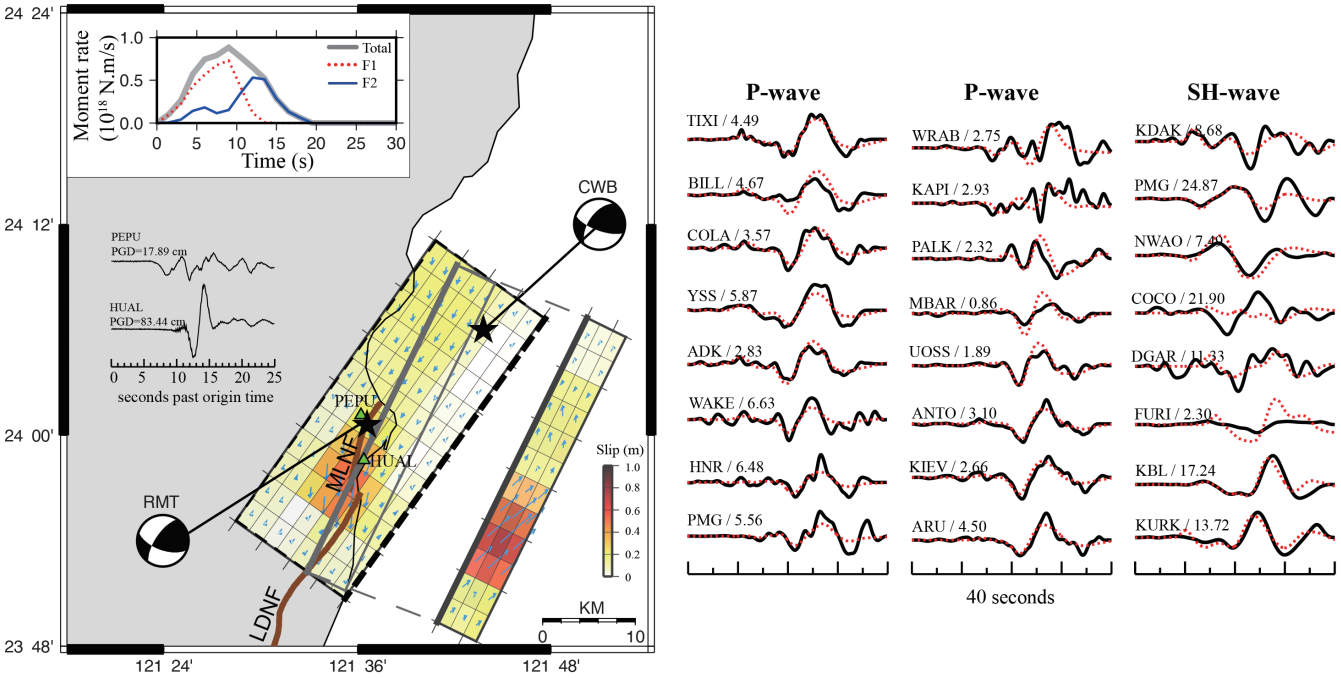

Fig. 7. Slip distribution of the preferred model and comparison of the observed (solid line) and the synthetic (dashed line) waveforms. The time series records of two high-rate continuous GPS stations (triangles) are also shown. The station name and peak value of the record in micrometers are shown above the teleseismic waveforms.

which is buried beneath the Longitudinal Valley fault for the northernmost LV (Shyu et al. 2005, 2006). Wen et al. (2019) suggested that the 2018 Hualien earthquake may be associated with a west-dipping blind fault which could reach out to the Heping sea basin and might belong to the Central Range fault. Figure 8 shows the locations of the 2000 Hualien event and its aftershocks, which correlate well with the 2018 Hualien mainshock and its aftershocks. On the other hand, McIntosh et al. (2005) suggested a west-dipping structure beneath the coastal and near shore area as a boundary between the sedimentary basin and continental crust, and the location is close to the west-dipping fault segment F1 of the 2018 Hualien earthquake. Further investigation of this not well-known structure should be carried out in the near future. Ohta et al. (2012) supposed that 11 March 2011 M_w 7.4 Sanriku-Oki earthquake aftershocks, which might be caused by strain concentration at the after-slip region edges, may have motivated nucleation for the 11 March 2011 M_w 9.0 Tohoku earthquake. Figure 1 shows that the 2018 Hualien mainshock initiated from the southern edge of the seismicity region following the M_w 6.1 event occurred two days before. The 2018 Hualien mainshock ruptured southward on both fault segments. Previous studies revealed that the strength and stress state of the fault, fault geometry and the fracture energy would strongly affect the rupture velocity during the faulting process (Rosakis 2002; Kanamori and Rivera 2006). One example is the slow rupture for the multifault of the 2016 Kaikoura earthquake (Wen et al. 2018). Therefore, for

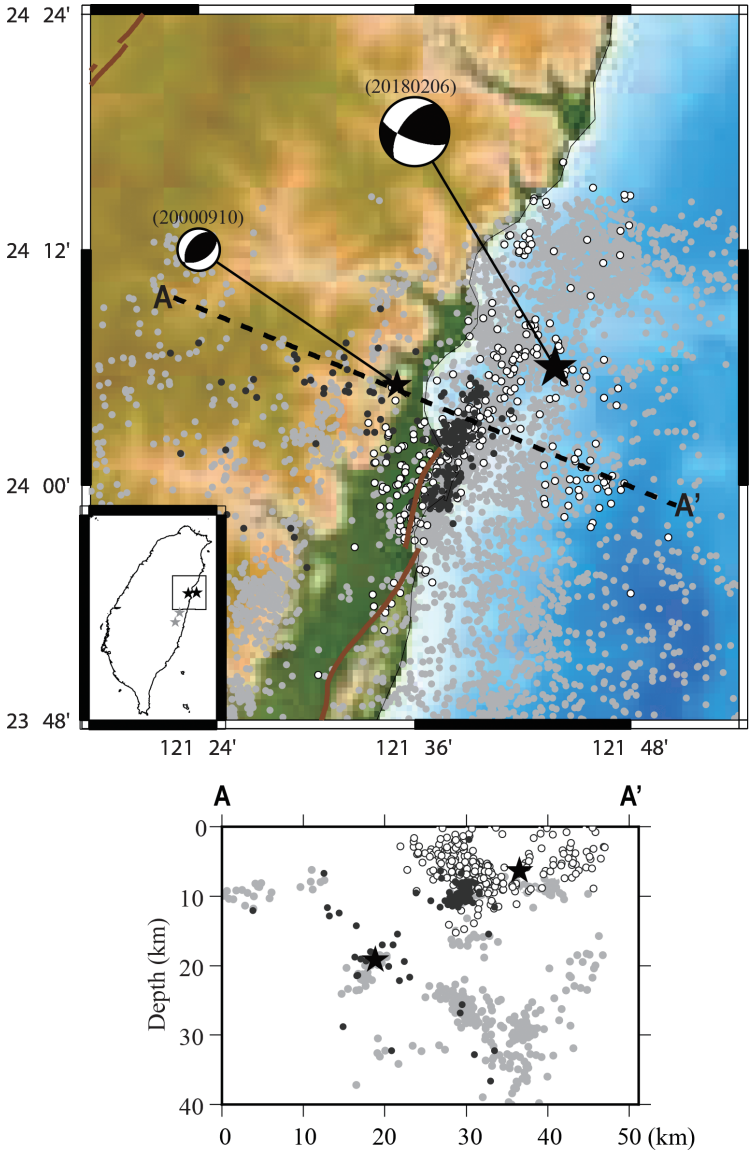

Fig. 8. Locations (black stars) and focal mechanisms of the 2000 and 2018 Hualien earthquakes, respectively. Gray stars show the locations of 2013 Ruisui and 2014 Fanglin earthquakes. Gray dots indicate background seismicity since 1990. Black and white dots represent the aftershock distributions of the 2000 and 2018 Hualien events, respectively.

the 2018 Hualien earthquake, stress transfer from the MLNF to LDNF would take some time to reach the critical status of rupture and thus slow down the propagation speed. The minor asperity with fast rupture velocity of 3.0 km s^{-1} on fault segment F1 might cause the directivity effect. On the other hand, main asperity with slow faulting speed of 2.0 km s^{-1} on the shallow fault segment F2 resulted in the surface rupture. The integrated effect might be the reason of serious damage for the 2018 Hualien earthquake. In the past few years, several moderate-sized events struck eastern Taiwan and caused strong ground shaking and some seismic damage, including 2013 Ruisui earthquake, 2014 Fanglin earthquake (Wen 2018; gray asterisks in Fig. 8), and the 2018 Hualien earthquake. The coincidence is that these events are considered occurring on the west-dipping fault. Are they all related to the Central Range fault? Why does this area become active recently? We should pay more attention and carry out more studies for this not well-known region.

Acknowledgements We thank editor Tai-Lin Tseng and two anonymous reviewers for their helpful comments. We thank the Geophysical Database Management System (http://gdms.cwb.gov.tw/index.php), developed by Central Weather Bureau (CWB) of Taiwan for providing seismic data. This research was supported by the Taiwan Earthquake Center (TEC) and funded through the Taiwan MOST grant MOST 106-2116-M-194-008 and 106-2116-M-194-011. The TEC contribution number for this article is 00147.

REFERENCES

Bassin, C., G. Laske, and G. Masters, 2000: The Current Limits of Resolution for Surface Wave Tomography in North America. *Eos, Trans., AGU*, **81**, F897.

Chen, K. H., S. Toda, and R.-J. Rau, 2008: A leaping, triggered sequence along a segmented fault: The 1951 M_L 7.3 Hualien-Taitung earthquake sequence in eastern Taiwan. *J. Geophys. Res.*, **113**, B02304, doi: 10.1029/2007JB005048. [Link]

Chen, W.-S., 2018: Investigation of the surface rupture for the 0206 Hualien earthquake. 20180206 Hualien Earthquake Workshop, CWB, Taipei, Taiwan. (in Chinese)

Chuang, R. Y., K. M. Johnson, Y. T. Kuo, Y. M. Wu, C. H. Chang, and L. C. Kuo, 2014: Active back thrust in the eastern Taiwan suture revealed by the 2013 Rueisuei earthquake: Evidence for a doubly vergent orogenic wedge? *Geophys. Res. Lett.*, **41**, 3464-3470, doi: 10.1002/2014GL060097. [Link]

Hsu, T. L., 1962: Recent faulting in the longitudinal valley of eastern Taiwan. *Mem. Geol. Soc. China*, **1**, 95-102.

Ji, C., D. J. Wald, and D. V. Helmberger, 2002: Source description of the 1999 Hector Mine, California, earthquake, Part I: Wavelet domain Inversion theory and resolution analysis. *Bull. Seismol. Soc. Am.*, **92**, 1192-1207, doi: 10.1785/0120000916. [Link]

Kanamori, H. and L. Rivera, 2006: Energy partitioning during an earthquake. In: Abercrombie, R., A. McGarr, H. Kanamori, and G. Di Toro (Eds.), Earthquakes: Radiated Energy and the Physics of Faulting, Geophysical Monograph Series, Vol. 170, American Geophysical Union, 3-13, doi: 10.1029/170gm03. [Link]

Kuo-Chen, H., F. T. Wu, and S. W. Roecker, 2012: Three-dimensional P velocity structures of the lithosphere beneath Taiwan from the analysis of TAIGER and related seismic data sets. *J. Geophys. Res.*, **117**, B06306, doi: 10.1029/2011JB009108. [Link]

Langston, C. A. and D. V. Helmberger, 1975: A procedure for modelling shallow dislocation sources. *Geophys. J. R. Astr. Soc.*, **42**, 117-130, doi: 10.1111/j.1365-246X.1975.tb05854.x. [Link]

Lawson, C. L., and R. J. Hanson, 1974: Solving Least Squares Problems, Prentice-Hall, Englewood Cliffs, NJ, 340 pp.

Lee, S.-J., L. Mozziconacci, W.-T. Liang, Y.-J. Hsu, W.-G. Huang, and B.-S. Huang, 2013: Source complexity of the 4 March 2010 Jiashian, Taiwan, Earthquake determined by joint inversion of teleseismic and near field data. *J. Asian Earth Sci.*, **64**, 14-26, doi: 10.1016/j.jseaes.2012.11.018. [Link]

McIntosh, K., Y. Nakamura, T.-K. Wang, R.-C. Shih, A. Chen, and C.-S. Liu, 2005: Crustal-scale seismic profiles across Taiwan and the western Philippine Sea. *Tectonophysics*, **401**, 23-54, doi: 10.1016/j.tecto.2005.02.015. [Link]

Ohta, Y., R. Hino, D. Inazu, M. Ohzono, Y. Ito, M. Mishina, T. Iinuma, J. Nakajima, Y. Osada, K. Suzuki, H. Fujimoto, K. Tachibana, T. Demachi, and S. Miura, 2012: Geodetic constraints on afterslip characteristics following the March 9, 2011, Sanriku-Oki earthquake, Japan. *Geophys. Res. Lett.*, **39**, L16304, doi: 10.1029/2012GL052430. [Link]

Rosakis, A. J., 2002: Intersonic shear cracks and fault ruptures. *Adv. Phys.*, **51**, 1189-1257, doi: 10.1080/00018730210122328. [Link]

Shyu, J. B. H., K. Sieh, Y.-G. Chen, and C.-S. Liu, 2005: Neotectonic architecture of Taiwan and its implications for future large earthquakes. *J. Geophys. Res.*, **110**, B08402, doi: 10.1029/2004JB003251. [Link]

Shyu, J. B. H., K. Sieh, Y.-G. Chen, and L.-H. Chung, 2006: Geomorphic analysis of the central range fault, the second major active structure of the longitudinal valley suture, eastern Taiwan. *GSA Bull.*, **118**, 1447-1462, doi: 10.1130/B25905.1. [Link]

Shyu, J. B. H., Y. R. Chuang, Y. L. Chen, Y. R. Lee, and C. T. Cheng, 2016: A new on-land seismogenic structure source database from the Taiwan Earthquake Model

(TEM) project for seismic hazard analysis of Taiwan. *Terr. Atmos. Ocean. Sci.*, **27**, 311-323, doi: 10.3319/TAO.2015.11.27.02(TEM). [Link]

Wen, S., Y.-Y. Wen, K.-E. Ching, Y.-L. Yeh, and Y.-H. Lee, 2019: Tectonic Implications on the 2018 Hualien Earthquake. *Terr. Atmos. Ocean. Sci.*, **30**, 389-398, doi: 10.3319/TAO.2019.01.28.01. [Link]

Wen, Y.-Y., 2018: Source Characteristics of the Northern Longitudinal Valley, Taiwan Derived from Broadband Strong-Motion Simulation. *Pure Appl. Geophys.*, **175**, 587-596, doi: 10.1007/s00024-017-1693-9. [Link]

Wen, Y.-Y., K.-F. Ma, and B. Fry, 2018b: Multiple-Fault, Slow Rupture of the 2016 M_w 7.8 Kaikōura, New Zealand, Earthquake: Complementary Insights from Teleseismic and Geodetic Data. *Bull. Seismol. Soc. Am.*, **108**, 1774-1783, doi: 10.1785/0120170285. [Link]